TU Delft

Delft University of Technology

Rolling pairs with shifting contact geometry
Design, development, and validation

Amoroso, Pedro; van Ostayen, Ron A.J.; de Rooij, Matthijn B.

DOI
10.1177/13506501241239490

Publication date
2024

Document Version
Accepted author manuscript

Published in
Proceedings of the Institution of Mechanical Engineers, Part J: Journal of Engineering Tribology

Citation (APA)
Amoroso, P., van Ostayen, R. A. J., & de Rooij, M. B. (2024). Rolling pairs with shifting contact geometry: Design, development, and validation. *Proceedings of the Institution of Mechanical Engineers, Part J: Journal of Engineering Tribology*. https://doi.org/10.1177/13506501241239490

Important note
To cite this publication, please use the final published version (if applicable).
Please check the document version above.

Copyright
Other than for strictly personal use, it is not permitted to download, forward or distribute the text or part of it, without the consent of the author(s) and/or copyright holder(s), unless the work is under an open content license such as Creative Commons.

Takedown policy
Please contact us and provide details if you believe this document breaches copyrights.
We will remove access to the work immediately and investigate your claim.

This work is downloaded from Delft University of Technology.
For technical reasons the number of authors shown on this cover page is limited to a maximum of 10.

Rolling Pairs With Shifting Contact Geometry: Design, Development, and Validation

Proc IMechE Part J: J Engineering Tribology
XX(X):1–17
©The Author(s) 2016
Reprints and permission:
sagepub.co.uk/journalsPermissions.nav
DOI: 10.1177/ToBeAssigned
www.sagepub.com/
SAGE

Pedro Amoroso[1,2*], Ron A.J. van Ostayen [1] and Matthijn B de Rooij[2]

Abstract

This work introduces two innovative rolling pair concepts to minimize slippage and reduce mass in cam-roller systems of large-scale hydraulic drivetrains: the Variable Contact Length (VCL) and the Shifting Contact Geometry (SCG) concepts. Both aim to improve traction in the low-contact force phase in cyclically loaded rolling contacts. The SCG concept was validated using three custom rolling contacts: a line contact, a double elliptical contact, and a combination of both (i.e., SCG). The tests were conducted under synchronized cyclic loading to mimic the conditions in a hydraulic drivetrain. Furthermore, a model from previous work was implemented to make predictions and compare them against the experimental results. During preliminary tests, the double elliptical contact displayed superior tractive behavior than the line contact under the same load thanks to higher contact pressures. Under synchronized cyclic loading, the line contact displayed high sensitivity to applied resisting torques at low contact forces, leading to high slide-to-roll ratios (SRRs) and traction force peaks. In contrast, the rolling pair with SCG exhibited minimum slippage even under high resisting torques, resulting in substantially lower (and in most cases negligible) SRRs and traction force peaks. The simulations also captured this behavior, proving the validity of the model for predicting and comparing the rolling-sliding dynamics of these two different rolling pairs. This study demonstrates that rolling pairs with SCG can not only improve the tribological performance of cam-roller contacts in large-scale hydraulic drivetrains but also yield a more favorable dynamic behavior.

Keywords

Large, scale, hydraulic, drivetrain, cam, roller, shifting, geometry, elliptical, line, rolling, sliding, slippage, traction.

Introduction

The development of reliable, low-maintenance, and low-mass systems for wind power generation is essential for reducing the levelized cost of offshore wind energy [1]. Over the recent years, a number of companies within the wind energy sector have focused their efforts on developing and incorporating fluid power technology in wind turbines in many different ways. This shift can be attributed to the robustness, compactness, and high power-to-mass ratio that characterize this technology [1,2].

For example, a promising solution is to replace the complex transmissions and electronics in current offshore turbines with a large-scale hydraulic drivetrain (HD), as proposed by the Delft Offshore Turbine (DOT) power train concept [3,4]. This HD is, in essence, a low-speed-high-torque multi-MW seawater piston pump that replaces the gearbox and generator in a regular wind turbine. The novel DOT concept is illustrated in Figure 1a, where a single water pump is directly connected to the rotor in the nacelle. The pump is designed to operate at a nominal water pressure of $420\,\mathrm{bar}$ with a displacement of roughly $400\,\mathrm{L}$ per revolution [4]. The pressurized water is transported to a central Pelton turbine, where the power production of multiple wind turbines is combined. This concept aims to reduce the top mass of the turbine (to reduce structural costs) and increase reliability (to reduce maintenance costs) by incorporating robust hydraulic components. As a result, the costs of an offshore wind turbine could be reduced by 25-50% [4].

Figure 1b shows the heart of the piston pump, where a camring and a set of radially arranged roller followers are used to carry out the pumping function. The camring is coupled to the rotor of the wind turbine (Figure 1a) and rotates counterclockwise, as shown in Figure 1c, thanks to the power generated by the wind, while the stator remains stationary. As the camring rotates, the roller followers convert the rotary motion into linear motion to pump the water inside the cylinders. Figure 1c highlights with pink, the cylinder units undergoing the water compression phase, and with blue, the ones in the suction phase. In the compression stroke, the water pressure in the cylinder increases sharply, and during the suction stroke, the pressure drops. During these two strokes, the cam-roller follower contacts are subjected to enormous fluctuating loads above $400\,\mathrm{kN}$.

From a tribological point of view, the cam-roller contacts in the HD are critical lubricated interfaces subjected to "countless" loading cycles and highly dynamic conditions

[1] Department of Precision and Microsystems Engineering, Delft University of Technology, Mekelweg 2, 2628 CD Delft, The Netherlands
[2]Faculty of Engineering Technology, University of Twente, Enschede, The Netherlands

Corresponding author:
Pedro Amoroso, Department of Precision and Microsystems Engineering, Delft University of Technology, Mekelweg 2, 2628 CD Delft, The Netherlands
Email: P.AmorosoFeijoo@tudelft.nl

over the pump's lifespan. At these interfaces, optimum lubrication must ensured for a smooth, reliable, and long-lasting operation.

In a recent theoretical study, the rolling-sliding performance of the roller followers in the pump was examined[5]. The results revealed that roller slippage occurs at low loads (during the suction stroke), but it rapidly disappears at high loads (during the compression stroke). This fast change in the rolling conditions results in high angular accelerations and given the size of the rollers, large inertia torques. Consequently, a sharp increase in the traction force is generated during this transition. These findings strongly suggest that slippage at the cam-roller interface should be minimized. By doing so, not only the tribological performance of the contacts would be improved, but also the overall dynamic behavior of the hydraulic drivetrain.

It is essential to point out that the behavior described above displays a striking resemblance to that of the rollers in large, slow-moving roller bearings carrying unidirectional loads[6,7]. In fact, the rolling-sliding behavior predicted in reference[5], exhibits a strong (qualitative) similarity to that shown in the experimental results obtained by Hamer et al.[7] for large-scale roller bearings. The reason for this is that both systems operate under similar dynamics. In large-scale roller bearings with unidirectional loads, the rollers also slip in the unloaded region and rapidly accelerate upon entering the high-load region[6–8]. Under these conditions, smearing damage (i.e., a form of adhesive wear) is likely to occur[9].

Taking into account the mass-reduction and tribological challenges described above, we have devised a unique and innovative out-of-the-box solution. Our patented idea aims to reduce mass and roller slippage simultaneously. In this work, we disclose and validate our proposed solution, which has led to the emergence of two novel rolling pair concepts: the Variable Contact Length (VCL) concept and the Shifting Contact Geometry (SCG) concept. We should highlight that our work focuses on introducing a novel rolling-pair concept designed specifically to reduce slippage and improve traction in systems that operate under varying synchronous loads. The cam-roller contacts in the previously mentioned HD serve as an ideal example to illustrate a possible application of our concept. Therefore, our solution is not limited to this particular case but may also be applicable and beneficial in other systems operating under similar conditions.

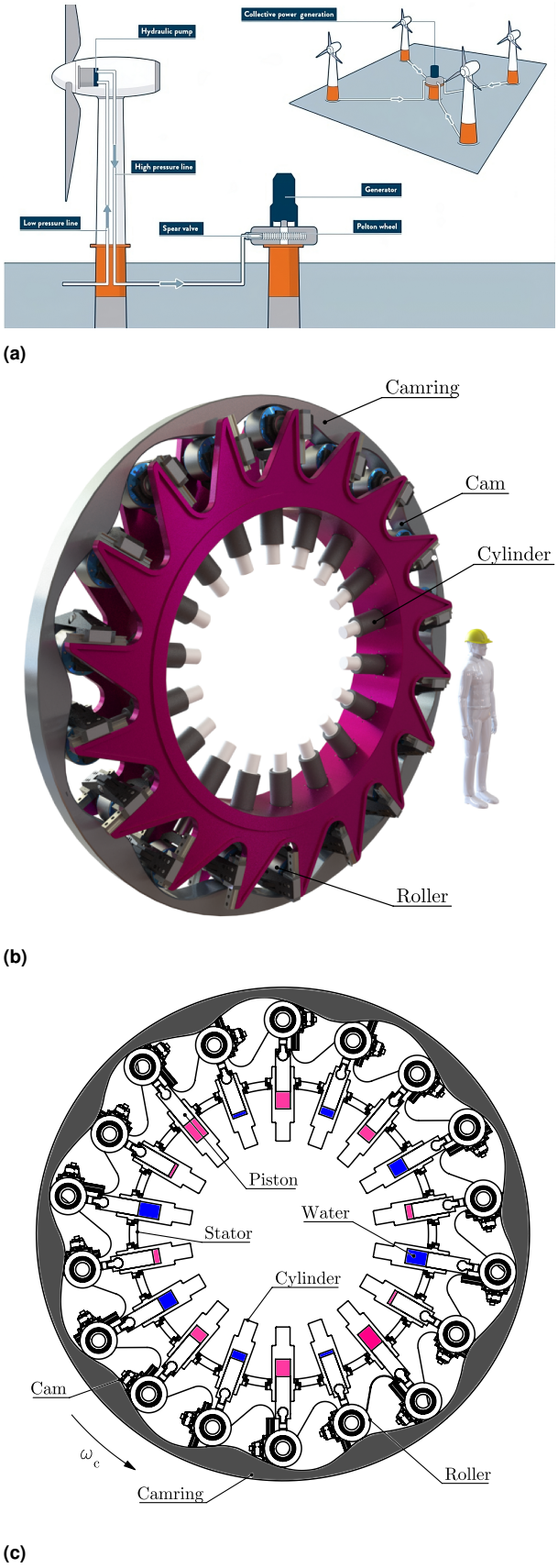

Figure 1. Application of the large-scale HD. (a) DOT3000 Power Train System Concept. (b) Large-scale HD. (c) Schematic of the HD operation.

The VCL and SCG Concepts

Cam-Roller Contacts in a HD

To gain a deeper insight into the Variable Contact Length (VCL) and Shifting Contact Geometry (SCG) concepts, it is crucial to dig into the circumstances from which these two concepts emerged. For that, we will refer to the results from reference[5]. Figure 2 depicts the rolling-sliding behavior of one cam-roller contact during one pumping cycle. During the compression and suction strokes, the contact force (F_c) and maximum contact pressure (P_{max}) at the cam-roller contact vary sharply (in a step-like fashion) as a function of the roller follower displacement (σ). High contact forces are generated during the compression stroke, as water is pressurized, and low contact forces during the suction stroke, as water is sucked into the cylinder. The remaining contact force during the suction stroke corresponds mainly to a preload applied

by a pneumatic spring[5]. Note that the maximum contact pressure P_{max} occurs at maximum displacement due to the increase in the curvature of the cam (Figure 1c). Figure 2 also shows the predicted slide-to-roll-ratio (SRR) and traction force (F_t) for one cam-roller contact in the large-scale HD[5].

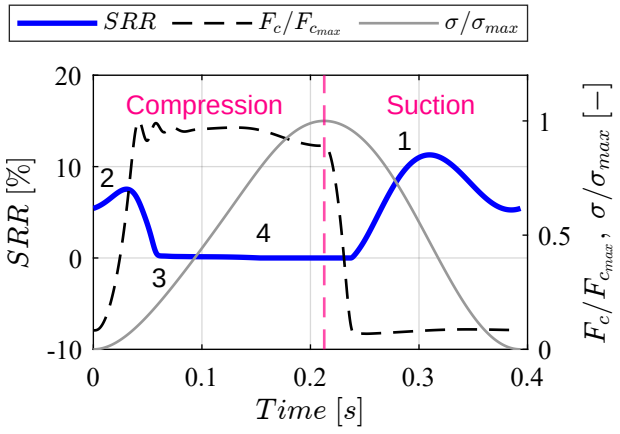

(a)

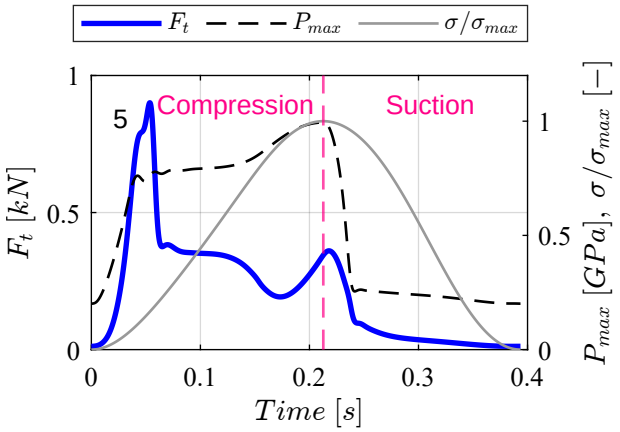

(b)

Figure 2. Rolling-sliding dynamics of cam-roller contacts in a large-scale hydraulic drivetrain (adapted from[5]).

In the two plots shown in Figure 2, 5 key characteristics have been highlighted. Figure 2a shows the predicted SRR profile. The SRR is equal to $(u_c + u_f)/u_m$, where u_c and u_f are the cam and roller follower surface velocities, respectively, and u_m is the lubricant's mean entrainment velocity. The SRR profile exhibits the following 4 key characteristics: (1) the roller slips during the low contact force phase, (2) the roller enters the high contact force phase with a noticeable level of slippage, (3) the roller rapidly transitions from rolling-sliding to virtually pure rolling, (4) the roller rolls without sliding under high contact forces, and then, the cycle repeats. The fifth (5) characteristic corresponds to the traction force peak highlighted in Figure 2b, which occurs as a result of the rapid change in the rolling conditions described above.

Description of the Idea

When looking for solutions to alleviate the behavior described above, it is reasonable to think of increasing the contact force to enhance traction. Nevertheless, increasing the preload would also result in higher contact forces during the compression phase. Consequently, the lifespan of bearings would be reduced, friction losses would increase, and rolling contact fatigue would be accelerated. Then, one could think of only increasing the contact force during the suction phase. However, this solution would most likely result in a complex actuation system, and still, extra loads.

In a rolling pair, the contact length and contact type are key parameters defining the contact area, and hence, the maximum contact pressure for a given contact force. Therefore, the decrease in contact pressure produced by the low contact forces in Figure 2b, can be attributed not only to the drop in contact force itself but also to an "over-dimensioned" contact area. In fact, if the loading conditions in a system are known, the length of the contact could be tailored to even up the contact pressure under a step-like highly-varying cyclic load. By leveling the contact pressure, traction can be improved, and roller slippage can be minimized. In addition, by modifying the contact length, the excess material can be removed and a substantial mass reduction could be attained. This is in essence the core of our idea, from which the VCL and SCG concepts emerged.

VCL and SCG Rolling Pairs

Figure 3 shows a schematic top-view of three different cam-roller follower configurations. To provide a clearer visual representation, Figure 4 shows the embodiment of these three different configurations in a large-scale HD. Figure 3a shows a conventional line-contact configuration, where the whole surface of the roller (1R) enters into contact with the cam. The cam has a section subjected to high contact forces (1C) and another section subjected to low contact forces (2C). In this case, these two sections have the same length and the line-contact geometry remains unchanged.

Figure 3b shows a top-view schematic of the VCL concept incorporated in the cam-roller contacts of a HD. The surface of the roller can be divided into two parts. Section 1R is in contact with the cam only during high-contact forces, whereas section 2R remains in contact under both, low and high-contact forces. In contrast to the conventional configuration (Figure 3a), the cam has a variable length. By continuously adapting its length to the given loading conditions, uniform contact pressures can be generated under cyclic loads. For this concept, the cam can be divided into the following sections: a section subjected to high contact forces (1C), a transition section from high to low contact forces (2C), a section subjected to low contact forces (3C), and a transition section from low to high contact forces (4C). Section 5C shows the excess material that could be removed. Although the VCL concept is very appealing from an idealistic point of view, its embodiment brings some challenges. One of them is the need for axial profiling in section 3C. This would be required to avoid edge effects at the extremes of section 2R, delimited by the two dashed lines (Figure 3b).

Figure 3c shows a top-view schematic of the SCG concept incorporated in the cam-roller contacts of a HD. This concept aims to reduce the manufacturing challenges foreseen for the VCL concept. In the SCG concept, the roller is divided into 3 actual sections, one single section (1R) and a double section (2R). Similarly, the cam has multiple sections: a section for

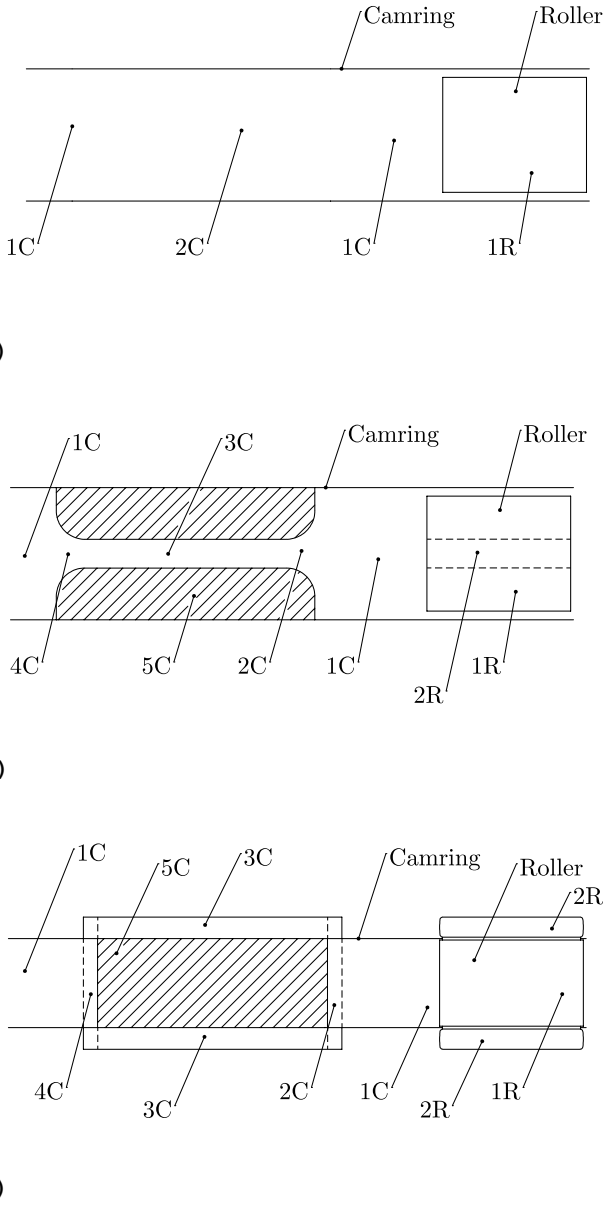

Figure 3. Three different rolling pair configurations. (a) Conventional line-contact. (b) VCL concept. (c) SCG concept.

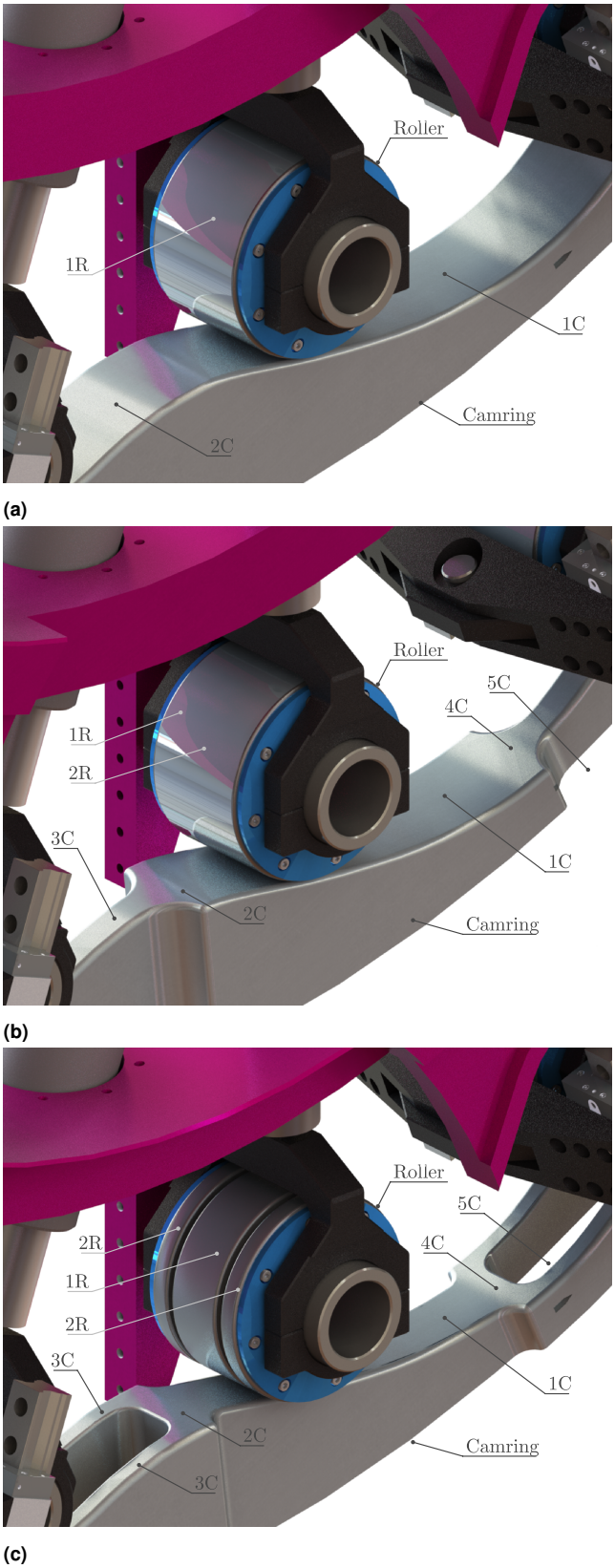

Figure 4. Three different cam-roller configurations in a large-scale HD. (a) Conventional line-contact. (b) VCL concept. (c) SCG concept.

high contact forces (1C), a transition section from low to high contact forces (2C), a double section for low contact forces (3C), and a transition section from low to high contact forces (4C). Section 5C shows the excess material that could be removed. Section 1R forms a line contact with 1C, which is required to take high contact forces. The double sections 2R and 3C take over at low contact forces forming a double elliptical contact. As a result, the contact area is reduced and contact pressure is increased, improving traction. During operation, the contacts shift in a "1-2-1 sequence" from a single line contact (1) to a double elliptical contact (2), and then, to a line contact (1) again.

Experimental Validation

Rolling Pair Design

As mentioned earlier, to further develop the VCL concept, section 3C (Figure 4b) would require accurate axial profiling

along the cam to prevent edge loading on the roller. For that reason, we have considered that rolling pairs with SCG are more attractive from the realization point of view, and therefore, we have directed our efforts to further develop and validate this concept. For that, a simplified small-scale approach has been followed. The cam-roller contact in the HD has been represented by using a two-roller configuration, where the bottom roller represents the cam and the top roller represents the roller follower.

Figure 5a shows 3 different rolling pairs designed for the experimental validation. The bottom rollers (R1) represent the cam. The subscripts F and SG stand for flat and shifting geometry, respectively. The top rollers (R2) represent the roller follower. The subscripts S, D, and T stand for single, double, and triple contact, respectively. The rolling pair $R2_S/R1_F$ forms a conventional line contact and $R2_D/R1_F$ a double elliptical contact. The last configuration, $R2_T/R1_{SG}$, is a rolling pair with SCG. The first two rolling pairs are used to evaluate the single-line contact and the double elliptical contacts independently. The last configuration is used to simultaneously evaluate a combination of both, i.e., a Shifting Contact Geometry (SCG).

The sections 1C and 3C in $R1_{SG}$ cover a $180°$ angle, respectively. Together, they form a perfectly round $360°$ circle. These two sections (1C and 3C) are the raceways for the sections 1R and 2R in $R2_T$, respectively. During rotation, these sections create the "1-2-1" shifting sequence described earlier. At 2C, the radii of 1C and 3C are the same, allowing for a smooth transition between the line and elliptical contact geometries (during rotation).

All the bottom (R1) and top (R2) rollers used for the validation experiments have a $54\,\mathrm{mm}$ diameter. The total length of R1 and R2 are $34\,\mathrm{mm}$ and $32\,\mathrm{mm}$, respectively. The line contact sections 1R in the rollers $R2_S$ and $R2_T$ have a straight length L_s of $11\,\mathrm{mm}$ and round edges with a $1.5\,\mathrm{mm}$ radius (Figure 5a). The elliptical contact sections 2R in rollers $R2_D$ and $R2_T$ have a $6\,\mathrm{mm}$ length and also round edges with a $1.5\,\mathrm{mm}$ radius. The remaining $3\,\mathrm{mm}$ at the center of these sections has a crowned profile with a $54\,\mathrm{mm}$ radius. In other words, the radii r_{2x} and r_{2y} of section 2R are $27\,\mathrm{mm}$ and $54\,\mathrm{mm}$, respectively, where x is aligned with the direction of rotation. For the $R1_{SG}$ roller, sections 1C and 3C have a length of $15\,\mathrm{mm}$ and $7.5\,\mathrm{mm}$, respectively. This implies that the quantity of material removed from the sides is equivalent to the quantity of material removed from the center. By doing so, the center of gravity remains aligned with the center of rotation. The material properties of these rollers are provided in section "Materials and Methods".

The Test Setup

Figure 5b shows the two-roller tribometer employed to validate our concept. A comprehensive description of this in-house developed test setup can be found in reference [10]. The bottom (1) and top (2) roller form the rolling pair under evaluation. The motor (3) drives the bottom roller at stable speeds. The magnetic hysteresis brake (4) is coupled to the top roller and is used to apply precise resisting torques on the top roller. In that way, different slip levels can be generated at the contact. The torque sensor (5) measures the torque τ_b applied by the brake. When velocity changes occur, the torque sensor also measures the inertia torque τ_i generated by the inertia on its right side. This inertia corresponds to a 98% of the total inertia I_t. A flywheel (6) is coupled to the brake to increase the effects of inertia under low speeds. The total inertia I_t added to R2 (including the flywheel inertia) is $1.45 \times 10^{-2}\,\mathrm{kg\,m^2}$. The two encoders (7a and 7b) are used to measure the rotational speed of the bottom and top rollers, respectively.

Synchronized cyclic loads are generated by using a sensing wheel (8) aligned with the angular position of the bottom roller and two proximity sensors (9a and 9b). Sensor 9b generates a switching signal that indicates whether the line or the elliptical contacts are operating. Sensor 9a is used for triggering a proportional pressure regulator valve with fast dynamic response (VPPM) that controls the pressure in the air bellow (10), and thus, the applied contact force. A load cell (11) located under the air bellow measures the applied contact force. Note that the top roller arm can compensate for titling, as indicated by the arrows in Figure 5a. This feature is intended to allow an even distribution of the load over the contacting surfaces.

Theoretical Validation

Predicting the rolling-sliding performance of different rolling pairs is highly valuable to support our experimental validation. For that, we have implemented a simple but effective approach that avoids the need for extensive simulations. A thorough description of the framework employed in this study can be found in reference [5]. For that reason, we will only discuss the most relevant aspects and nuances in this section.

Torque Balancing

Figure 6 shows a schematic of the forces and torques acting on the rollers in the test setup. The applied load generates a contact force F_c between the bottom (R1) and top (R2) rollers. R1 is driven by a torque τ_d at a stable speed ω_1. Thanks to the traction force F_t generated at the interface, R1 drives R2 (i.e., R1 is driving and R2 driven). The needle bearings (3), the flywheel (4), and the magnetic hysteresis brake (5) generate the resisting torques τ_f, τ_i and τ_b, respectively, which act on R2. The traction force F_t and the SRR developed at the interface depend on the sum of these torques.

The rotational speed of R2 (ω_2) is governed by the torque balance equation (eq. 1). This equation couples two tribological systems, the one formed by the test rollers, and the other by the needle bearings. This means that the frictional torque generated by the needle bearings affects the traction force F_t and the SRR developed at the contact between R1 and R2. Likewise, the frictional torque developed in the needle bearings depends on ω_2. This equation can be solved iteratively as shown in previous studies [5,11,12].

$$\tau_t = \tau_f + \tau_b + \tau_i \tag{1}$$

The tractive torque τ_t is equal to $F_c \mu r_2$, where μ is the traction coefficient and r_2 is the outer radius of R2. The traction force F_t is equal to $F_c \mu$. The frictional torque τ_f

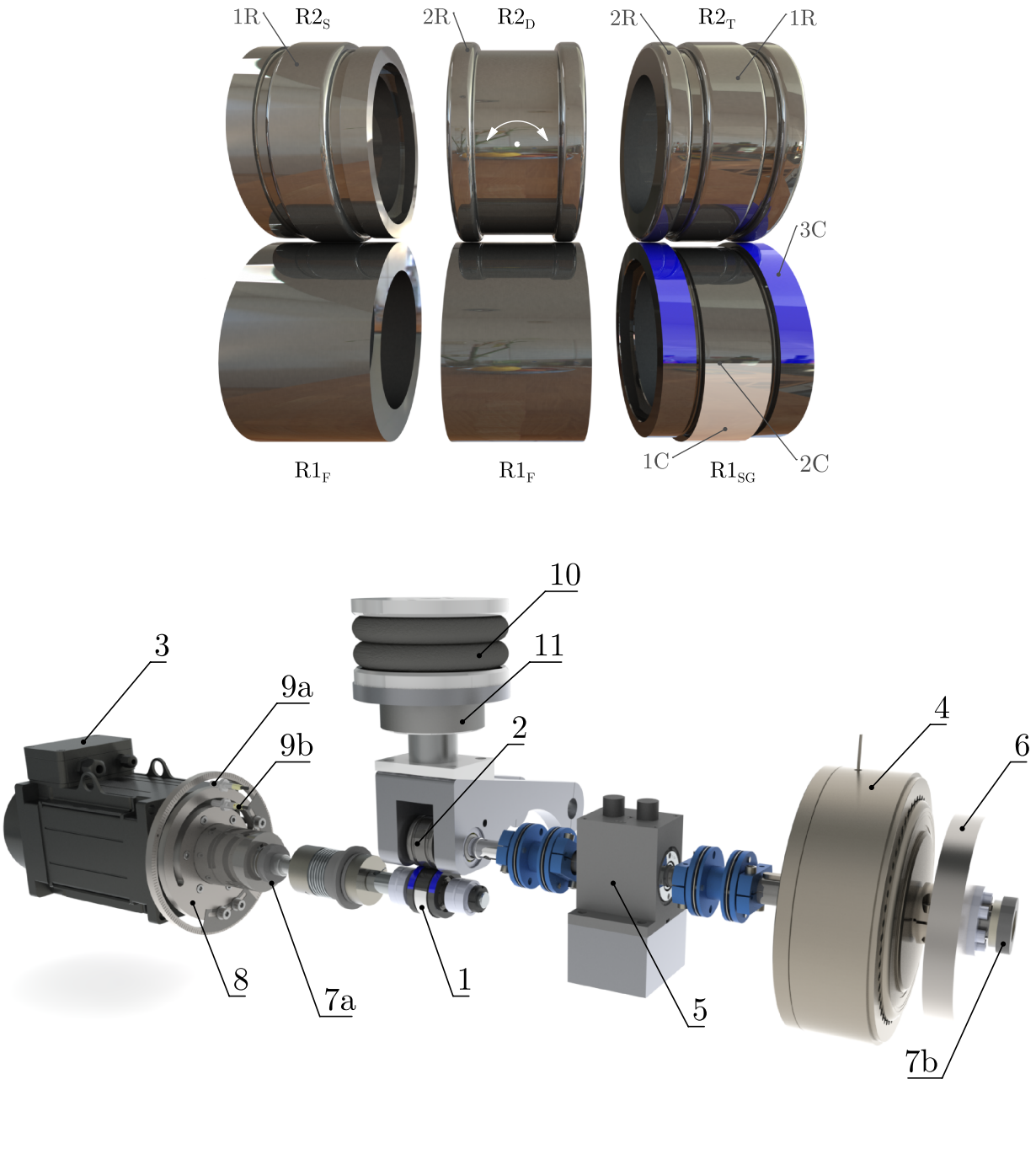

Figure 5. Experimental setup. (a) Test rollers. (b) Test setup. (R1) Bottom roller (1), (R2) top roller (2), motor (3), magnetic hysteresis brake (4), torque sensor (5), flywheel (6), encoders (7a and 7b), sensing wheel (8), proximity sensors (9a and 9b), air bellow (10), load cell (11).

is the sum of the frictional torques produced by two lateral needle bearings supporting the top roller shaft (Figure 5b). The inertia torque τ_i is equal to $I_t\dot{\omega}_2$, where I_t is the total inertia of the components rotating together with R2 and $\dot{\omega}_2$ is the angular acceleration of R2. By substituting these expressions in eq.1, the following expression is obtained:

$$F_c \mu r_2 = \tau_f + \tau_b + I_t\dot{\omega}_2 \quad (2)$$

To estimate the traction coefficient μ, the angular acceleration $\dot{\omega}_2$, and the frictional torque τ_f that balance eq. 2, two lubrication models have been coupled.

Estimation of the Traction Coefficient

The traction coefficient μ in eq. 2 is strongly dependent on the sliding velocity u_s, and thus, the SRR at the contact. In this case, u_s is equal to $|u_1 - u_2|$, where u_1 and u_2 are the tangential velocities of R1 and R2, respectively. The relation between μ and the SRR in a rolling contact is determined by

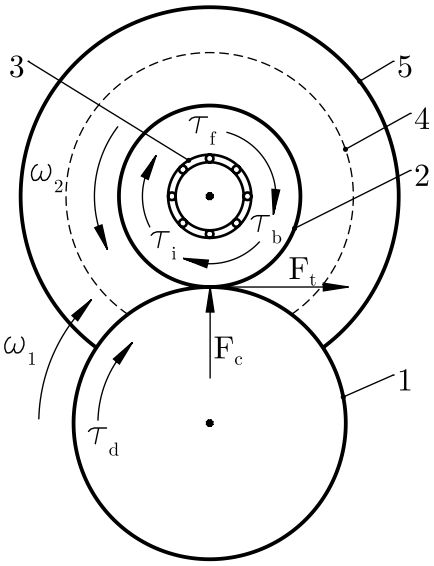

Figure 6. Forces and torques acting on the test rollers. Bottom roller (R1) (1), top roller (R2) (2), needle bearings (3), flywheel (4), brake (5).

its respective traction curve[13]. Therefore, when the RHS of eq. 2 increases, the traction coefficient μ must also increase to balance the expression. As dictated by the respective traction curve, an increase in the traction coefficient μ is attained when slippage occurs (i.e., when the sliding velocity u_s is different than zero). This behavior is also described as a "self-correcting action"[14].

Following the framework from reference[5], the traction coefficient μ can be evaluated with the traction and film thickness formulas provided by Masjedi and Khonsari[15]. For the rolling pairs with SCG, a pulse function (CG) switching from 0 to 1 is used to shift between the two types of contact depending on the acting contact geometry (CG) in a discrete way. The switching CG value (i.e., the type of contact) is generated by the proximity sensor 9b (Figure 5b) during the experiments. As a result, the traction coefficients are calculated as follows:

$$\mu = \begin{cases} \mu^L; \text{ if } CG = 1 \\ \mu^E; \text{ if } CG = 0 \end{cases} \quad (3)$$

where the superscripts ^{L} and ^{E} are used for the line and elliptical contact, respectively. Since we have conducted the experiments under full film lubrication, the expressions in reference[15], to compute the traction coefficients μ^L and μ^E, can be reduced to:

$$\mu^L = \frac{F_t^L}{F_c} = \frac{A^L \tau_{\text{lim}}^L}{F_c}\left[1 - \exp\frac{-\eta_{\text{avg}\,L} u_s}{\tau_{\text{lim}}^L h_c^L}\right] \quad (4)$$

$$\mu^E = \frac{2F_t^E}{F_c} = \frac{2A^E \tau_{\text{lim}}^E}{F_c}\left[1 - \exp\frac{-\eta_{\text{avg}\,E} u_s}{\tau_{\text{lim}}^E h_c^E}\right] \quad (5)$$

where A is the Hertzian contact area, τ_{lim} is the limiting shear stress for the lubricant, η_{avg} is the average viscosity (calculated as per the Roelands equation in reference[15]), and h_c is the central film thickness. Note that in eq.5, the contact force F_c has been divided by 2, since F_c is distributed over 2 elliptical contacts, as shown in Figure 5a.

Although we acknowledge the modifications proposed by Xi et al.[16] to improve eq.5, we have decided to use this expression as it is. This decision is justifiable because these modifications[16] result in better estimations under low SRRs and mixed lubrication conditions. However, in our study, the experiments have been conducted under full-film lubrication. For the rolling pairs with SCG, high contact pressures are maintained, and therefore, the contacts operate in the elastic-piezoviscous (E-P) regime. Nevertheless, for the conventional line contact, particularly under low contact pressures, the operating conditions move closer to the rigid-piezoviscous (R-P) boundary and near the elastic-isoviscousv (E-I) boundary.

The lubrication regime has been determined by the lambda ratio $\lambda = h_{min}/\sigma^*$, where h_{min} is the minimum film thickness (calculated with the expressions in reference[15]) and σ^* is the composite surface roughness. The composite surface roughness is given by $(Rq_{R1}^2 + Rq_{R2}^2)^{1/2}$, where Rq_{R1} and Rq_{R2} are the root mean square roughness parameters for the bottom (R1) and top (R2) rollers, respectively.

Estimation of Frictional Torque

The framework in reference[5], uses the SKF model[17] to estimate the frictional torque produced by the spherical roller bearings. In contrast, we have implemented the empirical expression derived by Chiu & Myers[18] that is suited for the needle bearings in our test setup (Figure 5b). This expression accounts for the viscous and load-dependent bearing torque and neglects seal friction. Since the bearings in the CRT (Figure 5b) have an open design, there is no need to account for the latter.

The frictional torque generated by each needle bearing can be calculated as:

$$\tau_{f1} = 4.5 \cdot 10^{-10} \nu_0^{0.3} d_m n^{0.6} + 1.2^{-4} d_m (0.5F_c)^{0.41} \quad (6)$$

where, ν_0 is the reference kinematic viscosity of the lubricant, d_m is the mean bearing diameter, and n is the bearing speed (in rpm). Note that the force acting on each bearing is $0.5F_c$. Since the traction force F_t is small when compared to F_c, it does not cause significant changes in the frictional torque (Figure 6). Hence, its influence has been neglected. The mean bearing diameter values (d_m) used in eq.6 for each bearing are 31 mm and 28.5 mm.

Materials & Methods

In this section, the reference conditions and methodology required to reproduce our experimental and theoretical results are provided.

Material and Lubricant Properties

The test rollers R1 and R2 are made of high-strength chromium-molybdenum alloy steel. The top roller (R2) was nitrocarburized to improve its hardness. The material properties, including the elastic modulus (E_{R1} and E_{R2}), Poisson's ratio (ν_{R1} and ν_{R2}), and the hardness (HV_{R1} and

HV_{R2}), are detailed in Table 1. All rollers were polished to achieve a surface roughness of approximately $Rq \approx 0.1\,\mu m$. The surface roughness was measured using an optical microscope Sensofar S Neox 3D profiler in confocal mode, employing 10x magnification.

During the experiments, the test rollers were placed in an oil bath and lubricated with high-viscosity (ISO-VG 680) mineral oil. This lubricant was used in the experiments for conservative reasons, to ensure that wear could be entirely avoided even at such low speeds (e.g., 60 rpm), and where nearly full sliding conditions occurred (e.g., Figure 7a). All the experiments were conducted at 20 °C (room temperature). Thus, the inlet temperature T_0, was assumed to be 20 °C as well. The needle bearings were lubricated with grease composed of a calcium sulphonate complex thickener (CaS) with a polyalphaolefin (PAO) base oil. The dynamic (η) and kinematic (ν) viscosities at 40 and 100 °C for the mineral oil and PAO, respectively, were provided by the supplier. The temperature assumed to estimate the kinematic viscosity ν_0 in eq.6 was 20 °C as well. The viscosity at the reference temperature (20 °C) was estimated according to the ASTM standard [19].

For the mineral oil, the limiting shear stress coefficient Λ_{min}, was obtained from Mini Traction Machine (MTM) measurements. The density ρ_{lub}, at 20 °C, was also provided by the supplier. The pressure viscosity coefficient α, the viscosity-temperature coefficient β, and the viscosity-pressure index Z were estimated with the expressions provided in reference [20] (Table 1). Note that Table 1 also contains the values for specific heat C_{pR1} and C_{pR2}, thermal conductivity k_{R1} and k_{R2}, as well as the density of steel ρ_{R1} and ρ_{R2}. These properties are required for estimating the temperature rise during the evaluation of the traction coefficient μ [15]. The interested reader is referred to reference [15], where the use of these properties is described in detail.

Table 1. Material and lubricant properties.

Parameter	Value	Unit
E_{R1}, E_{R2}	210	GPa
ν_{R1}, ν_{R2}	0.33	–
k_{R1}	46	$W\,m^{-1}\,K^{-1}$
k_{R2}	21	$W\,m^{-1}\,K^{-1}$
$C_{p_{R2}}, C_{P_{R2}}$	450	$J\,kg^{-1}\,K^{-1}$
ρ_{R1}, ρ_{R2}	7800	$kg\,m^{-3}$
HV_{R1}	2.17	GPa
HV_{R2}	6.36	GPa
Rq_{R1}	0.1	µm
Rq_{R2}	0.1	µm
T_0	20	°C
$\nu_{40\,°C}$	100	$mm^2\,s^{-1}$
$\nu_{100\,°C}$	13.4	$mm^2\,s^{-1}$
ν_0	293.77	$mm^2\,s^{-1}$
ρ_{lub}	900	$kg\,m^{-3}$
$\eta_{40\,°C}$	0.625	Pa s
$\eta_{100\,°C}$	0.039	Pa s
η_0	3.04	Pa s
α	28.8	GPa^-1
β	0.048	–
Λ_{min}	0.076	–
Z	0.525	–

Torque-Mode Traction Tests

To generate a traction curve in torque mode, the contact force F_c and the speed of the bottom roller ω_1 is maintained fixed, the braking torque τ_b is gradually increased in small steps (from low to high), and the resulting SRR is recorded. To construct the curves, the average SRR can be plotted against the average applied braking torque τ_b. This methodology, originally developed for cam-roller contacts, is described in reference [10], and is suitable for assessing the sensitivity of an interface to an applied resisting torque [10–12].

In a preliminary validation stage, we conducted a set of traction tests in torque mode. This allowed us to independently evaluate the tractive performance of a single line contact ($R2_S/R1_F$) and a double elliptical contact ($R2_D/R1_F$) under the same (low) load, but different contact pressures.

The experiments were conducted with the 2 rolling pairs described above, at 3 different speeds (60, 180 and 360rpm). Each experiment was conducted with a 0.475 kN load, resulting in a maximum Hertzian contact pressure $P^L_{max} = 0.34$ GPa (for the single line contact), and $P^E_{max} = 1$ GPa (for the double elliptical contact). Table 2, summarizes the reference conditions for 6 different torque-mode traction test.

Table 2. Reference conditions for torque-mode traction tests.

Test	Rolling pair	Load / P_{max}	Speed (R1)
$a1$	$R2_S/R1_F$	0.475 kN / 0.34 GPa	60rpm
$a2$	$R2_D/R1_F$	0.475 kN / 1 GPa	60rpm
$b1$	$R2_S/R1_F$	0.475 kN / 0.34 GPa	180rpm
$b2$	$R2_D/R1_F$	0.475 kN / 1 GPa	180rpm
$c1$	$R2_S/R1_F$	0.475 kN / 0.34 GPa	360rpm
$c2$	$R2_D/R1_F$	0.475 kN / 1 GPa	360rpm

Synchronized Cyclic Loading Experiments

The synchronized cyclic loading experiments were designed to mimic the rolling-sliding dynamics of the cam-roller contacts in the HD (Figure 2). As mentioned above, the test setup can apply loads that are synchronized with the angular position of the bottom roller (R1), which represents the cam. In that way, approximately half of the bottom roller is subjected to high loads and the other half to low loads. These loading conditions are comparable to those experienced by the lobes of a cam in a HD. These experiments aimed to evaluate the performance of both, a rolling pair with a conventional line contact ($R2_S/R1_F$), and a rolling pair with a novel SCG ($R2_T/R1_{SG}$), under the same conditions. By doing so, we could demonstrate how a rolling pair with SCG can drastically reduce slippage, and consequently, improve the rolling-sliding dynamics.

Initially, we intended to generate cyclic loads ranging from a minimum of 0.475 kN to a maximum of 4 kN, which would yield a 1 GPa maximum contact pressure for the elliptical and line contacts, respectively. However, due to limitations in the response time of the pneumatic actuation system, we lowered the maximum load to only 2.65 kN. As a result, the transition time from low to high loads was reduced from approximately 0.5 s to 0.28 s. This change was convenient to speed up the change from low to high load and vice-versa.

Reducing the maximum contact force reduced the maximum contact pressure for the line contact to $0.82\,\mathrm{GPa}$. However, this contact pressure proved to be sufficient to generate a rapid transition in the rolling conditions, capture important dynamic effects, and validate our concept.

Considering the response time constraints mentioned earlier, we limited the speed of R1 to 60rpm. This decision is rooted in the fact that the angular position of R1 dictates the load transitions, and higher rotational speeds would hinder the pneumatic system from keeping pace with the switching signals triggered by the proximity sensors (Figure 5b). Consequently, the intended characteristics of the cyclic load, including its magnitude, position, and timing, would not be maintained. In simpler terms, synchronization would be lost.

Under low loads and low contact pressures, rolling contacts are highly sensitive to an applied resisting torque[5,10–12]. This means that under these conditions, a very small increment in the resting torque can lead to a sharp increase in the SRR. To emphasize this aspect and simulate different scenarios, 4 different braking torques τ_b (ranging from low to high) were applied during the experiments, resulting in 4 experiments for each rolling pair, and hence, 8 experiments in total. Table 3 summarizes the reference conditions for all the synchronized cyclic loading experiments.

Given that the speed of R1 was kept stable at 60rpm, the duration of a loading cycle (comprised of a high contact force phase and a low contact force phase) was $1\,\mathrm{s}$. In other words, the frequency of the cyclic load was $1\,\mathrm{Hz}$. To complete a total of 600 loading cycles, the duration of each experiment was set to $10\,\mathrm{min}$.

For each experiment, the data corresponding to 600 cycles was processed to obtain the average cycle for the contact force F_c, maximum contact pressure P_{max}, slide-to-roll ratio SRR, and traction force F_t. By doing so, the significance of the results was improved and remarkably smooth plots were generated. Hence, further data filtering or smoothing was unnecessary.

Table 3. Reference conditions for synchronized cyclic loading experiments.

Experiment	Rolling pair	Load range	τ_b
$a1$	$R2_S/R1_F$	$0.475-2.65\,\mathrm{kN}$	$0.07\,\mathrm{N\,m}$
$b1$	$R2_S/R1_F$	$0.475-2.65\,\mathrm{kN}$	$0.60\,\mathrm{N\,m}$
$c1$	$R2_S/R1_F$	$0.475-2.65\,\mathrm{kN}$	$0.85\,\mathrm{N\,m}$
$d1$	$R2_S/R1_F$	$0.475-2.65\,\mathrm{kN}$	$1.00\,\mathrm{N\,m}$
$a2$	$R2_T/R1_{SG}$	$0.475-2.65\,\mathrm{kN}$	$0.07\,\mathrm{N\,m}$
$b2$	$R2_T/R1_{SG}$	$0.475-2.65\,\mathrm{kN}$	$0.60\,\mathrm{N\,m}$
$c2$	$R2_T/R1_{SG}$	$0.475-2.65\,\mathrm{kN}$	$0.85\,\mathrm{N\,m}$
$d2$	$R2_T/R1_{SG}$	$0.475-2.65\,\mathrm{kN}$	$1.00\,\mathrm{N\,m}$

Results and Discussion

Torque-Mode Traction Tests

Figures 7a, 7b, and 7c show the torque-mode traction test results at 60, 180, and 360rpm. The plots present the applied braking torque τ_b versus the SRR and relative SRR reduction percentage $(Red.)$, calculated as $(SRR^L - SRR^E)/SRR^L * 100$. The tests reveal that the double elliptical contact consistently outperforms the line contact in terms of traction, showing less sensitivity to the applied braking torques and maintaining lower SRRs. As will be discussed in the following sections, reducing the sensitivity of the rolling interface at low loads is beneficial to minimize slippage and improve the dynamic behavior of the contact. The impact of increased sensitivity of a line contact under dynamic loads can be seen in, for example, Figure 8d, where large SRRs and high traction force peaks are generated.

The SRR reduction attained with the double elliptical contact $(Red.)$ exceeds 50% across all speeds, becoming more pronounced at higher speeds, with nearly 100% reduction at 360rpm. This improvement is attributed to higher contact pressures and the rheology of the lubricant under elastohydrodynamic lubrication, where increased pressure enhances the traction coefficient. These findings underscore the benefits of optimizing contact pressure in full film lubrication to improve traction performance, which is significantly influenced by the pressure viscosity and limiting shear stress characteristics of the lubricant.

Table 4. Maximum and minimum predicted lambda ratios line-contact.

Experiment	Max. $\lambda\,[-]\,/\,T[\mathrm{s}]$	Min. $\lambda\,[-]\,/\,T[\mathrm{s}]$
L(a1)	16.95 / 0.90	14.88 / 0.29
L(b1)	16.34 / 0.80	14.84 / 0.28
L(c1)	16.17 / 0.77	14.48 / 0.03
L(d1)	16.07 / 0.74	12.98 / 0.04

Synchronized Cyclic Loading Experiments

Rolling Pair With a Conventional Line-Contact. Figure 8a, 8b, 8c, and 8d show the results of the synchronized cyclic loading experiments for a conventional line-contact with braking torques τ_b equal to $0.07\,\mathrm{N\,m}$, $0.60\,\mathrm{N\,m}$, $0.85\,\mathrm{N\,m}$, and $1.00\,\mathrm{N\,m}$, respectively. Table 4 shows the minimum and maximum lambda ratios λ predicted for the conventional line-contact together with the position (in seconds) at which they are expected to occur. These values have been calculated assuming a composite surface roughness σ^* equal to $0.14\,\mu\mathrm{m}$. For experiments a1 to d1, the maximum lambda ratios are expected at low contact forces (before the onset of slippage), due to the decrease in contact pressure. For experiments a1 and b1, the minimum lambda ratios are expected at the highest contact force. However, for experiments c1 and d1, the minimum lambda ratios are expected at maximum SRRs.

In Figure 8, the plots on the left show the average contact force F_c and slide-to-roll ratio SRR profiles, while the plots on the right show the average maximum Hertzian contact pressure P_{max} and traction force F_t profiles. These profiles represent the averaged results from 600 loading cycles, which in turn corresponds to 600 rotations of the bottom roller (R1). Additionally, the slide-to-roll ratio SRR^* and traction force F_t^* profiles predicted by the model implemented in this work are also shown for comparison. Note that the superscript "*" has been used to differentiate the predictions from the measurements.

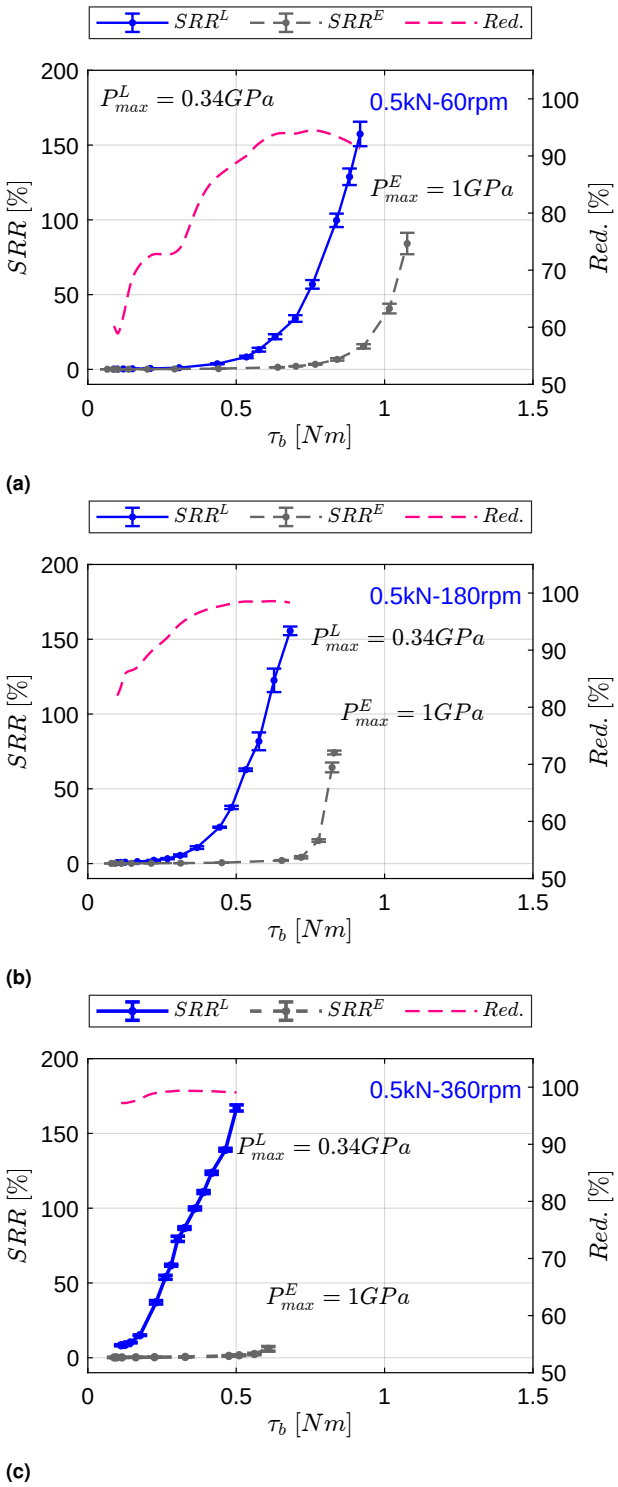

Figure 7. Torque-mode traction curves. (a) 60rpm. (b) 180rpm. (c) 360rpm.

First, it is important to highlight how our methodology allows us to mimic the rolling-sliding dynamics of cam-roller contacts in a large-scale HD. Taking Figure 8b as an example, (where slippage occurs), the 5 key characteristics mentioned earlier (Figure 2) can be observed. (1) The roller slips during the low contact force phase, (2) the roller enters the high contact force phase with a noticeable SRR, (3) the roller rapidly transitions from rolling sliding to virtually pure rolling, and (4) the roller rolls without sliding. The fifth characteristic (5) related to the peak in the traction force profile can be seen in the plot on the right.

In contrast to the traction force profile in Figure 2, the peaks observed in the traction force profiles in Figures 8b, 8c, and 8d are succeeded by a sequence of oscillations that gradually decline over time. These oscillations are captured by our test setup when a large inertia is added to the top roller. Their origin can be attributed to the variations in the angular acceleration that arise as the top roller attempts to match its surface speed to that of the bottom roller during the so-called "self-correcting" action [14], as discussed earlier. The generation of such dynamics is unattainable in traditional two-disc experiments, and we consider this a captivating aspect for future research.

Figure 8a shows that at low braking torques τ_b slippage is minimal, and therefore, angular accelerations become negligible. Consequently, no peaks in the traction force profile are produced. In contrast, Figures 8b, 8c, and 8d show that even with a slight increase in the braking torque, large SRRs are generated. Particularly, during the low contact force phase. As described earlier, this occurs as a result of the high sensitivity of the line contact interface caused by the drop in contact pressure.

The occurrence of slippage leads to the generation of high traction force peaks and their magnitude is directly proportional to the SRRs generated during the low contact force phase. In other words, the more slippage there is during the low contact force phase, the higher the traction force peak generated at the beginning of the high contact force phase. This can be attributed to larger angular accelerations generated during the abrupt transition from rolling-sliding to virtually pure rolling.

Overall, for the conventional line contact, the experimental and theoretical results show good agreement. The theoretical approach effectively captures predominant trends and yields reasonable results. The model demonstrates its capability to predict with acceptable accuracy the magnitude, shape, and position of relevant features within the SRR and traction force profiles. Including the oscillations that follow the peak traction force. Therefore, we believe that the predictions obtained with the framework employed in this work provide valuable insights into the rolling-sliding dynamics of line contacts subjected to cyclic loads. It is important to note that the disparities between the predictions and measurements could, in part, be attributed to the absence of precise pressure-viscosity coefficient data. Additionally, although the sliding velocities u_s were very low, a slight increase in the inlet temperature during the experiments may have played a role as well. While the inlet temperature T_0 in the model is assumed to be 20 °C, a slight temperature increase is likely to have occurred at large SRRs. In fact, we observed a better match between the predicted and measured SRRs for the experiments $c1$ and $d1$ (Table 3), assuming that the inlet temperature T_0 increased to 21 °C for $c1$, and then to 22 °C for $d1$, respectively. Although such temperature rise is likely to have occurred at large SRRs, we decided to maintain the inlet temperature T_0 at 20 °C, since we are uncertain about this change.

Table 5 shows the maximum measured (SRR) and predicted (SRR^*) slide-to-roll ratios together with the position (in seconds) at which they occur. Note that in all

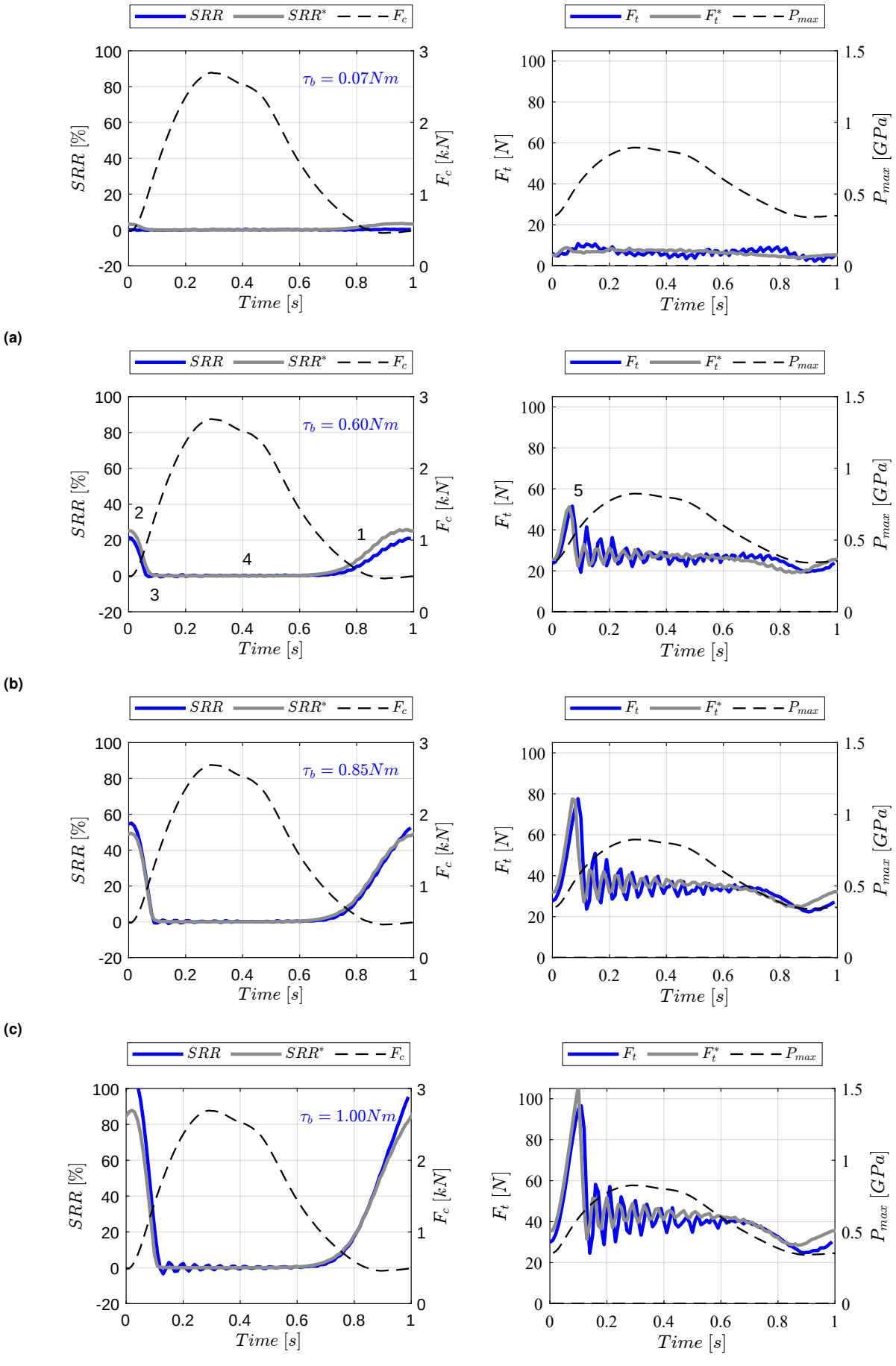

Figure 8. Rolling-sliding performance of a rolling pair with a single line contact under synchronized cyclic loading. (a) $\tau_b = 0.07\,\mathrm{N\,m}$, (b) $\tau_b = 0.60\,\mathrm{N\,m}$, (c) $\tau_b = 0.85\,\mathrm{N\,m}$, (d) $\tau_b = 1.00\,\mathrm{N\,m}$.

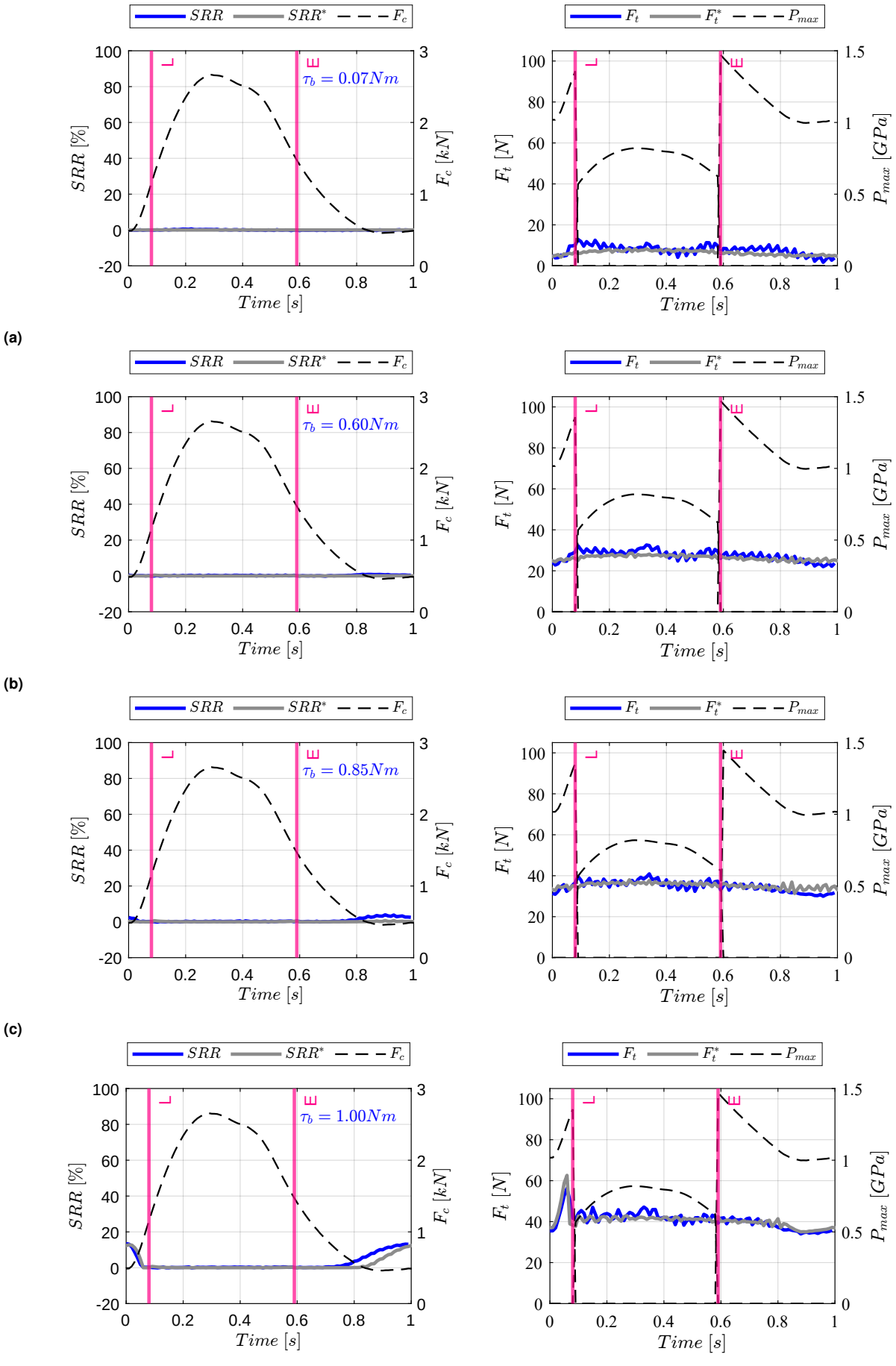

Figure 9. Rolling-sliding performance of a rolling pair with SCG under synchronized cyclic loading. (a) $\tau_b = 0.07\,\mathrm{N\,m}$, (b) $\tau_b = 0.60\,\mathrm{N\,m}$, (c) $\tau_b = 0.85\,\mathrm{N\,m}$, (d) $\tau_b = 1.00\,\mathrm{N\,m}$

cases, the maximum SRRs are expected to occur at the end of the cycle, which can also be practically seen as the beginning of a new cycle. For the conventional line contact, the positions at which the maximum SRRs occur are in line with the measurements. Table 6 contains the maximum measured (F_t) and predicted (F_t^*) traction forces for the conventional line contact together with the position (in seconds) at which they occur. Note that the predicted traction forces are in close agreement with the measurements in terms of magnitude and position.

Table 5. Maximum measured and predicted (*) SRRs for the conventional line-contact.

Experiment	SRR [%] / T [s]	SRR^* [%] / T [s]
L(a1)	0.50 / 0.90	3.63 / 0.96
L(b1)	21.44 / 0.00	25.76 / 0.98
L(c1)	55.04 / 0.01	49.41 / 0.01
L(d1)	105.73 / 0.02	87.85 / 0.02

Table 6. Maximum measured and predicted (*) traction forces for the conventional line-contact.

Experiment	F_t [N] / T [s]	Ft^* [N] / T [s]
L(a1)	10.87 / 0.09	8.87 / 0.05
L(b1)	51.57 / 0.07	51.29 / 0.06
L(c1)	77.60 / 0.09	77.45 / 0.07
L(d1)	96.53 / 0.11	106.74/ 0.10

Rolling Pair with SCG. Figure 9a, 9b, 9c, and 9d show the results of the synchronized cyclic loading experiments for a rolling pair with SCG with braking torques τ_b equal to $0.07\,\mathrm{N\,m}$, $0.60\,\mathrm{N\,m}$, $0.85\,\mathrm{N\,m}$, and $1.00\,\mathrm{N\,m}$, respectively. Table 7 summarizes the maximum and minimum predicted lambda ratios λ for the rolling pair with SCG, together with the position (in seconds) at which they are expected to occur. Likewise, these values have been calculated assuming a composite surface roughness σ^* equal to $0.14\,\mu\mathrm{m}$. For experiments a2 to d2, the maximum lambda ratios are expected during the low-to-high contact force transition, where the line contact is slightly "underloaded". In contrast, the minimum lambda ratios for experiments a2 to d2 are expected to occur during the high-to-low contact force transition. At this instant, the elliptical contact is slightly "overloaded".

Table 7. Maximum and minimum predicted lambda ratios for the rolling pair with SCG.

Experiment	Max. λ [$-$] / T[s]	Min. λ [$-$] / T[s]
SCG(a2)	15.77 / 0.09	11.50 / 0.59
SCG(b2)	15.75 / 0.09	11.49 / 0.59
SCG(c2)	15.76 / 0.09	11.53 / 0.60
SCG(d2)	15.71 / 0.09	11.50 / 0.59

In Figure 9, the plots on the left show the average contact force F_c and slide-to-roll ratio SRR profiles, while the plots on the right show the average maximum contact pressure P_{max} and traction force F_t profiles. These profiles also represent the averaged results from 600 cycles. The slide-to-roll ratio SRR^* and traction force F_t^* predicted by the framework adopted in this work are also included for comparison. As explained earlier, the superscript "*" has been used to differentiate the predictions from the measurements.

In addition, the vertical lines (L and E) located at approximately 0.1 and $0.6\,\mathrm{s}$, indicate the shift from one contact geometry to another. During a $0.5\,\mathrm{s}$ time frame from 0.1 to $0.6\,\mathrm{s}$, the single line contact is subjected to high loads. At time $0.6\,\mathrm{s}$, the double elliptical contact takes over for $0.4\,\mathrm{s}$ (from 0.6 to $1\,\mathrm{s}$) to finish the cycle, and it remains in operation at the beginning of a new cycle for $0.1\,\mathrm{s}$ (from 0 to $0.1\,\mathrm{s}$). After that, the single line contact takes over again, following the "1-2-1" sequence described earlier.

As mentioned in the previous section, our methodology effectively reflects the rolling-sliding dynamics expected in larger-scale applications. Despite the time scale differences, the experimental technique employed establishes a setting that facilitates the straightforward and controlled testing and validation of the SCG concept in an engineering sound manner.

Even though the testing conditions remain the same, the rolling-sliding dynamics of a rolling pair with SCG are entirely different from that of a conventional line contact. As shown in the plots on the right, high contact pressures are generated during the low contact force phase, when the double elliptical contact takes over. Consequently, traction can be drastically improved under low loads, and hence, the SRR can be minimized. Even at larger resisting torques (e.g., $0.85\,\mathrm{N\,m}$), the rolling pair with SCG maintains low SRRs when compared to the single-line contact. It is only at $1\,\mathrm{N\,m}$ (Figure 9d) that the SRR increases to approximately 13.4%, leading to a peak of around $56\,\mathrm{N}$ in the traction force. In contrast, under these conditions (i.e., $\tau_b = 1\,\mathrm{N\,m}$), the maximum SRR for the conventional line contact reaches approximately 106%, and it generates a traction force peak of roughly $97\,\mathrm{N}$ (Figure 8d).

Overall, for the double elliptical contact, the experimental and theoretical results show moderate agreement. By looking at the plots in Figure 9, it can be seen that the model captures the trends of relevant features within the SRR and traction force profiles. However, some estimations were somewhat less accurate than those for the line contact, particularly at small SRRs. For example, as shown in Table 8, for experiments a2 and b2, the predictions differ from the measurements in terms of magnitude and position. For the experiments a2 and b2, the model predicts that the maximum SRR occurs at $0.09\,\mathrm{s}$. At this instant, the line contact takes over and it is slightly "underloaded". Nevertheless, the measurements showed something different. For experiment a2, the maximum SRR occurred a little after the line contact took over (i.e., $0.22\,\mathrm{s}$), and for b2 when the elliptical contact is in operation (i.e., $0.82\,\mathrm{s}$). For experiment c2, the model predicts the position of the maximum SRR with accuracy, but the magnitude is off. For experiment d2, both, the position and magnitude of the maximum SRR are captured with good accuracy. Table 9 shows the maximum measured (F_t) and predicted (F_t^*) traction forces for the rolling pair with shifting contact geometry. In all cases, there is good agreement in terms of the predicted magnitudes. However, for experiments a2, b2, and c2, the predicted positions differ since there is no obvious traction force peak in the profiles. In contrast, for experiment d2, the predictions are in good agreement with the measurements in terms of position and magnitude, since in this case a traction force peak was generated.

Table 8. Maximum measured and predicted (*) SRRs for the rolling pair with SCG.

Experiment	SRR [%] / T [s]	SRR^* [%] / T [s]
SCG(a2)	0.60 / 0.22	0.09 / 0.09
SCG(b2)	0.85 / 0.82	0.43 / 0.09
SCG(c2)	3.92 / 0.90	0.72 / 0.90
SCG(d2)	13.44 / 0.00	12.79 / 0.01

Table 9. Maximum measured and predicted (*) traction forces for the rolling pair with SCG.

Experiment	F_t [N] / T [s]	Ft^* [N] / T [s]
SCG(a2)	12.90 / 0.09	8.35 / 0.29
SCG(b2)	32.60 / 0.33	28.57 / 0.28
SCG(c2)	40.91 / 0.34	38.02 / 0.27
SCG(d2)	56.21 / 0.06	62.59 / 0.06

It is worth noting that, as previously stated, the modeling approach used in this study simplifies the transition between contact geometries assuming that it occurs discretely. In reality, the shift from one contact geometry to another is more complex than that. For example, during the transition, both the double elliptical contact and the line contact operate together for a few milliseconds. The transient effects associated with such transition are rather challenging to detect experimentally and numerically. Besides, we have adapted an expression for a single elliptical contact to evaluate traction in a double elliptical contact. Perhaps, some differences arise from such simplification. For example, during the experiments, a small disparity in the load applied to each elliptical contact may explain the larger SRRs recorded for all the experiments. Nevertheless, despite the inconsistencies at low SRRs, the modeling approach remains valuable, since it detects the limits of the SCG configuration at high braking torques (e.g., Figure 9d).

From an engineering perspective, the framework utilized in this study has been considered appropriate for rapidly assessing and contrasting the rolling-sliding dynamics of the SCG concept with that of a conventional line contact. The effectiveness of the SCG concept is evident when comparing Figures 8 and 9, Tables 5 and 8, and Tables 6 and 9, respectively. Therefore, we believe that the modeling framework implemented in this work can come in handy during the design phase to quickly assess and compare the performance of rolling pairs with SCG against that of a conventional line contact.

From the observed behavior, we can derive the conclusion that rolling pairs featuring SCG not only enhance the tribological performance but also exhibit much more favorable dynamics. This observation holds particular significance for large-scale rolling contacts subject to highly varying cyclic loads, such as the cam-roller systems found in large-scale HDs. While slippage at low loads under film lubrication might initially seem harmless, it is the abrupt change in the rolling conditions and the resulting peaks in traction force that could potentially pose a concern. In fact, this behavior is also observed in unidirectionally loaded large-slow-moving roller bearings, where smearing damage remains an issue[6–9].

It is crucial to emphasize that our validation demonstrates the feasibility of integrating two separate types of contact within a single rolling pair. This approach effectively enhances the tribological performance, particularly under highly fluctuating (synchronous) loads, and it is not limited to this specific application. The SCG concept can be beneficial in other applications with similar operating conditions (e.g., [11,21]). Our findings confirm that it is feasible to switch between contact geometries, each designed to operate under determined loading conditions. This also means that these two independent tribological contacts could be customized to optimize their performance under a given set of conditions. For example, different materials, surface finishes, coatings, and even lubricants could be used to get the most out of each contact geometry. To conclude this section, Figure 10 shows the different rolling pairs employed in this work to conduct the validation experiments.

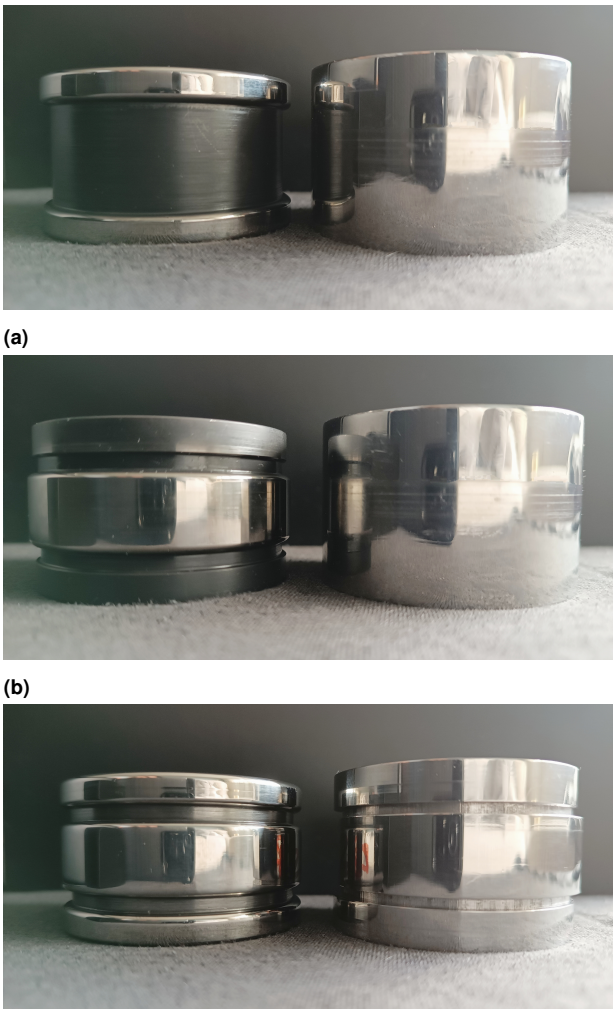

Figure 10. Three different rolling pair configurations. (a) Double elliptical contact. (b) Line contact. (c) SCG.

Conclusions

In this study, an innovative solution to address mass reduction and roller slippage in cam-roller systems for large-scale HDs has been introduced. We have presented our idea, which gave rise to two novel rolling pair concepts: the Variable Contact Length (VCL) and the Shifting Contact Geometry (SCG) concepts. Both concepts were devised to

level up the contact pressure under varying cyclic loads. By doing so, traction has been improved under low contact forces. We should emphasize that the application of the proposed novel rolling pair concepts extends beyond the cam-roller contacts in the HD discussed in this study. In fact, it has the potential to be useful and beneficial in other systems operating under highly fluctuating synchronous loads where slip remains a concern (e.g., [11,21]). The cam-roller contacts in the HD simply serve as an ideal example where we have illustrated where our concept could be incorporated.

The SCG concept was further developed for validation due to its apparent feasibility. To ensure practicality and cost-effectiveness, validation experiments were simplified and scaled down. For that, an existing two-roller test setup was upgraded to generate synchronized cyclic loads. These experiments involved three custom-designed rolling pairs: one with a line contact, another with a double elliptical contact, and the last with a combination of both (i.e., with a SCG). Additionally, we employed a modeling framework from previous work to make predictions and compare them with experimental results.

In the preliminary validation stage, we compared the tractive performance of a single line contact to that of a double elliptical contact under the same load and at different speeds. The double elliptical contact consistently outperformed the line contact, offering reduced sensitivity to applied resisting torques and a significant reduction in the slide-to-roll ratio (SRR). This enhancement was attributed to the lubricant's pressure-viscosity characteristics.

For the SCG concept validation, experiments were conducted under synchronized cyclic loading conditions, effectively simulating cam-roller contact dynamics in a large-scale hydraulic drivetrain. The conventional line contact displayed high sensitivity to applied resisting torques and led to high SRRs and traction force peaks. These traction force peaks were succeded by a sequence of oscillations which we consider a captivating aspect for future research. The generation of such dynamics can not be attained in conventional two-disc tests. In contrast, the SCG rolling pair significantly minimized slippage even under high braking torques, resulting in lower SRRs and traction force peaks. These results strongly confirmed the validity of our concept which can not only reduce slippage but also yield more favorable dynamic performance.

Overall, predictions and experimental results were well aligned, indicating the effectiveness of the modeling framework. However, disparities were partly attributed to the lack of precise pressure-viscosity coefficient data and potential temperature variations during experiments. The inconsistencies observed for the SCG concept, may be a result of transient effects during the transition from one contact geometry to another. These effects cannot be captured by the model, as it assumes a discrete transition from one contact geometry to another. Additionally, an uneven distribution of load over the double elliptical contact during the experiments was considered another possible cause.

In summary, the SCG concept introduces a "new dimension" by allowing two discrete contact geometries within a single rolling pair. This feature enables designers to independently tailor these tribological systems to achieve a desired performance under specific conditions. For future work, we expect to explore various aspects, such as different materials, surface finishes, coatings, and lubricants to further optimize the performance of each contact geometry.

Declaration of Conflicting Interests

The author(s) declared no potential conflicts of interest with respect to the research, authorship, and/or publication of this article.

Funding

The authors disclosed receipt of the following financial support for the research, authorship, and/or publication of this article: The research presented in this paper is part of the DOT3000 project, which was conducted by Delft University of Technology in collaboration with Delft Offshore Turbine (DOT) and executed with funding received from the Dutch ministry of economic affairs via TKI Wind at Sea, Top sector Energy, project number [TEHE119007].

References

1. Thomsen KE, Dahlhaug OG, Niss MOK, Haugset SK. Technological advances in hydraulic drive trains for wind turbines. Energy Procedia. 2012;24:76-82.
2. Chen W, Wang X, Zhang F, Liu H, Lin Y. Review of the application of hydraulic technology in wind turbine. Wind Energy. 2020;23(7):1495-522.
3. Diepeveen N. On fluid power transmission in offshore wind turbines [PhD thesis]. Delft University of Technology; 2013.
4. Grow. Growth through Research, development & demonstration in Offshore Wind. Grow; 2019. [Cited 2023 Sep 5]. Available from: https://grow-offshorewind.nl/project/dot3000-pts.
5. Amoroso P, van Ostayen RAJ, Perassi F. Rolling-Sliding Performance of Radial and Offset Roller Followers in Hydraulic Drivetrains for Large Scale Applications : A Comparative Study. MDPI Machines. 2023;11(6):604.
6. Hamer JC. An Experimental Investigation Into the Boundaries of Smearing Failure in Roller Bearings. Journal of Tribology. 1991;113(1):102-19.
7. Hamer C. Smearing in Rolling Element Bearings [PhD thesis]. University of London; 1991.
8. Evans RD, Barr TA, Houpert L, Boyd SV. Prevention of Smearing Damage in Cylindrical Roller Bearings. Tribology Transactions. 2013;56(5):703-16.
9. Rowe FD. Diagnosis of rolling contact bearing damage. Tribology. 1971;4(3):137-46.
10. Amoroso P, Vrček A, Rooij MD. A Novel Tribometer and a Comprehensive Testing Method for Rolling-Sliding Conditions. MDPI Machines. 2023;11(11):1-19.
11. Alakhramsing SS, de Rooij MB, Schipper DJ, van Drogen M. A full numerical solution to the coupled cam–roller and roller–pin contact in heavily loaded cam–roller follower mechanisms. Proceedings of the Institution of Mechanical Engineers, Part J: Journal of Engineering Tribology. 2018 10;232(10):1273-84.
12. Alakhramsing SS, de Rooij MB, Akchurin A, Schipper DJ, van Drogen M. A mixed-TEHL analysis of cam-roller contacts

considering roller slip: On the influence of roller-pin contact friction. Journal of Tribology. 2019 1;141(1).
13. Johnson KL, Cameron R. Fourth Paper: Shear Behaviour of Elastohydrodynamic Oil Films at High Rolling Contact Pressures. Proceedings of the Institution of Mechanical Engineers. 1967;182(1):307-30.
14. Ji F, Taylor CM. A tribological study of roller follower valve trains. Part 1: A theoretical study with a numerical lubrication model considering possible sliding. Tribology Series. 1998;34:489-99.
15. Masjedi M, Khonsari MM. An engineering approach for rapid evaluation of traction coefficient and wear in mixed EHL. Tribology International. 2015 7;92:184-90.
16. Xi Y, Björling M, Shi Y, Mao J, Larsson R. Traction formula for rolling-sliding contacts in consideration of roughness under low slide to roll ratios. Tribology International. 2016 12;104:263-71.
17. SKF Group. The SKF model for calculating the frictional moment; 2018. [Cited 2023 Oct 30]. Available from: https://cdn.skfmediahub.skf.com/api/public/0901d1968065e9e7/pdf_preview_medium/0901d1968065e9e7_pdf_preview_medium.pdf.
18. Chiu YP, Myers M. A rational approach for determining permissible speed for needle roller bearings. SAE Technical Papers. 1998;107:330-7.
19. ASTM International. Standard Test Method for Viscosity-Temperature Charts for Liquid Petroleum Products. ASTM; 2004.
20. Khonsari MM, Booser ER. Applied Tribology: Bearing Design and Lubrication, 3rd Edition. 3rd ed. 2017 John Wiley & Sons Ltd; 2017.
21. Li S, Guo F, Sun N, Zhu G, Chao S, Liu X. Elastohydrodynamic lubrication analysis of cam-roller pairs of internal combustion engines. International Journal of Engine Research. 2023;24(4):1374-87.

Appendix

Notation

A	Hertzian contact area	m^2
α	Pressure viscosity coefficient	GPa^{-1}
β	Viscosity-temperature coefficient	-
$C_{p_{R1,R2}}$	Specific heat	$\mathrm{J\,kg^{-1}\,K^{-1}}$
d_m	Mean bearing diameter	mm
$E_{R1,R2}$	Young's modulus	GPa
E'	Effective Young's modulus	GPa
F_c	Contact force	N
F_t	Traction force	N
η	Dynamic viscosity	$\mathrm{Pa\,s}$
η_{avg}	Average viscosity	$\mathrm{Pa\,s}$
h_c	Central film thickness	$\mu\mathrm{m}$
h_c	Minimum film thickness	$\mu\mathrm{m}$
$HV_{R1,R2}$	Vickers hardness	GPa
I_t	Total inertia	$\mathrm{kg\,m^2}$
k	Ellipticity parameter	-
$k_{R1,R2}$	Thermal conductivity	$\mathrm{W\,m^{-1}\,K^{-1}}$
L_s	Straight contact length	m
λ	Lambda ratio	-
Λ_{min}	Limiting shear stress coefficient	-
μ	Traction coefficient	-
μ_E	Traction coefficient (elliptical contact)	-
μ_L	Traction coefficient (line contact)	-
ν	Kinematic viscosity	$\mathrm{mm^2\,s^{-1}}$
$\nu_{R1,R2}$	Poisson's ratio	-
n	Needle bearing speed	rpm
P_{max}	Max. Hertzian contact pressure	GPa
$\rho_{R1,R2}$	Density	$\mathrm{kg\,m^{-3}}$
ρ_{lub}	Lubricant density	$\mathrm{kg\,m^{-3}}$
r_2	R2 outer radius	m
$R1$	Bottom roller	-
$R2$	Top roller	-
R'	Equivalent contact radius	m
$Rq_{R1,R2}$	Root mean square roughness	$\mu\mathrm{m}$
SRR	Slide-to-roll ratio	-
σ	Roller follower displacement	m
σ^*	Composite surface roughness	m
T	Time	s
T_0	Inlet temperature	$^\circ\mathrm{C}$
u_c	Cam surface velocity	$\mathrm{m\,s^{-1}}$
u_1	R1 tangential speed	$\mathrm{m\,s^{-1}}$
u_2	R2 tangential speed	$\mathrm{m\,s^{-1}}$
u_m	Mean entrainment velocity	$\mathrm{m\,s^{-1}}$
u_f	Roller surface velocity	$\mathrm{m\,s^{-1}}$
u_r	Rolling velocity	$\mathrm{m\,s^{-1}}$
u_s	Sliding velocity	$\mathrm{m\,s^{-1}}$
τ_b	Braking torque	$\mathrm{N\,m}$
τ_d	Driving torque	$\mathrm{N\,m}$
τ_f	Frictional torque	$\mathrm{N\,m}$
τ_i	Inertia torque	$\mathrm{N\,m}$
τ_t	Tractive torque	$\mathrm{N\,m}$
τ_{lim}	Limiting shear stress	Pa
$\dot{\omega}_2$	R2 angular acceleration	$\mathrm{rad\,s^{-2}}$
ω_1	R1 rotational speed	$\mathrm{rad\,s^{-1}}$
ω_2	R2 rotational speed	$\mathrm{rad\,s^{-1}}$